Characterisation of the flow around passenger vehicle wheels with varying tyre profiles

International Journal of Heat and Fluid Flow 103 (2023) 109191

Contents lists available at ScienceDirect

International Journal of Heat and Fluid Flow

journal homepage: www.elsevier.com/locate/ijhff

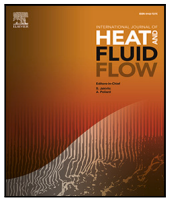

Characterisation of the flow around passenger vehicle wheels with varying tyre profiles

Erik Josefsson [a,*], Simone Sebben [a], Magnus Urquhart [b]

[a] Department of Mechanics and Maritime Sciences, Chalmers University of Technology, 412 96 Gothenburg, Sweden
[b] Aerodynamics, Volvo Cars, 418 78 Gothenburg, Sweden

ARTICLE INFO

Keywords:
Vehicle aerodynamics
Wheels
Tyre profiles
Drag
Wind tunnel

ABSTRACT

The flow around wheels contributes to a significant part of the aerodynamic drag of passenger vehicles, which is crucial for overall energy efficiency. The rotation and bluff-body geometry of the wheels result in a complex flow field that is sensitive to geometrical variations such as the tyre geometry, tread pattern, tyre deformation and rim design.

In this work, wind tunnel tests were performed with a full-scale crossover SUV, using two rim configurations and three tyres. Utilising flow field measurements and time-resolved surface pressure measurements, the main features of the flow were identified for three sets of tyres with distinct shoulder profiles and sidewall geometry. The main differences were found close to the ground. With a narrower sidewall, a smaller contact patch vortex was formed, reducing the drag. Combining the narrow sidewall with a narrow tread, the more rounded shoulder created a larger contact patch vortex and pronounced the vortex from the outer downstream tyre shoulder.

Comparing closed and open rims, the same overall flow mechanisms were observed but their relative importance was altered. An interaction between the tyre and rim design was found, mainly in terms of how the front wheel wakes affect the rear wheels.

1. Introduction

With new emission regulations and customer expectations of increased electric vehicle range there is a need for improving the energy efficiency of vehicles. Around 20−30% of the traction power is required to overcome aerodynamic drag (Pavlovic et al., 2016), making the drag an important factor for the total energy consumption. For a passenger vehicle, the wheels contribute to approximately a quarter of the drag (Cogotti, 1983; Wickern et al., 1997), making tyre and rim design an area of interest for investigation. Factors such as the wheels' bluff-body geometry and rotation result in a complex flow field that is challenging to simulate and comprehend.

Fackrell and Harvey (1973) were among the first to investigate wheels, showing experimentally how rotation affects the flow field of an isolated wheel, focusing on the pressure distribution. They identified the jetting phenomena, where the pressure coefficient can exceed one upstream of the contact patch due to the energy added to the flow by the rotation. Later research, such as Croner et al. (2013), Patel et al. (2022) and Parfett et al. (2022), investigated both the time-averaged and instantaneous flow fields, mainly with respect to the vortices. The studies highlighted the importance of the ground vortices created at either side of the contact patch, showing how they affect the wake.

Although studies of isolated wheels provide insights into the fundamental flow features, they do not account for the effects of encapsulating the wheels in a vehicle body. The vehicle geometry will result in a yawed oncoming flow at the front wheels, as shown by Wiedemann (1996). The effect of yaw on an isolated wheel was considered by Parfett et al. (2022) and was found to significantly change the wake structures compared to the unyawed case, increasing the strength of the leeward ground vortex and decreasing the strength of its windward counterpart. Additionally, a yawed flow was found to stabilise the large fluctuations found at zero yaw. This dependence on the flow angle highlights the importance of considering the wheel in combination with the vehicle geometry.

Wäschle (2007) compared isolated and encapsulated wheels in both stationary and rotating conditions, showing that the encapsulation alters the flow mechanisms. Fig. 1 shows the vortex structures for a rotating encapsulated wheel. Downstream of the tyre, a wake horseshoe is found (A). At the ground, a strong outer contact patch vortex (B) is formed along with vortex pair C, caused by the separation at the downstream tyre shoulder. Due to the yawed flow, C_{in} is stronger than C_{out}. Vortex D is caused by the rim flange. The lower part is fed by the flow through the rim and should therefore be dependent on the

* Corresponding author.
E-mail addresses: erik.josefsson@chalmers.se (E. Josefsson), simone.sebben@chalmers.se (S. Sebben), magnus.urquhart@volvocars.com (M. Urquhart).

https://doi.org/10.1016/j.ijheatfluidflow.2023.109191
Received 9 March 2023; Received in revised form 7 June 2023; Accepted 25 June 2023
Available online 6 July 2023

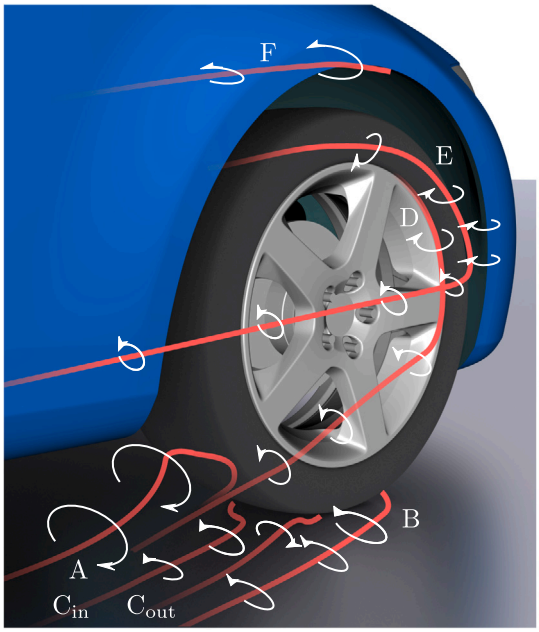

Fig. 1. Vortex structures for a rotating wheel. *Source:* Adapted from Josefsson et al. (2022), inspired by Wäschle (2007).

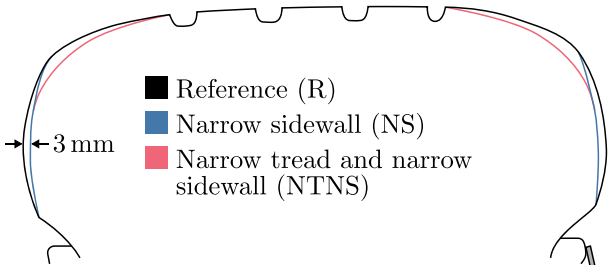

Fig. 2. Schematic drawing of the tyre profiles. The thickness of the rim cover is illustrated in grey in the bottom right corner.

(a) Open rim (b) Closed rim

Fig. 3. Investigated rims.

rim design. With the rotating tyre, the separation at the tyre shoulder results in vortex E. Leakages from the top of the wheelhouse create vortex F.

Wittmeier et al. (2013, 2014) investigated how the drag was affected by the tyre profile. The main influence was found at the front wheels, where edges or sharp angles at the tyre shoulder were detrimental. Due to the angle of the incoming flow and the shielding from the wheelhouse, the most important region was the lower part of the outer shoulder, where differences in shoulder radius altered the size of the contact patch vortex (B). It was also found that there can be a strong synergy between the tyre profile and the rim design. With a sharp shoulder profile the flow separated already at the tyre, reducing the influence of the rim.

This work aims at increasing the knowledge of the effects of tyre shoulder and sidewall geometry on the aerodynamics of a full-scale passenger vehicle. Although simplified scale models are often used to investigate fundamental flow features, they lack important details such as deflectors and suspension. Additionally, due to the importance of the tyre deformation (Mlinaric, 2007; Landström et al., 2012; Gray et al., 2019), full-scale testing is preferable. Wind tunnel measurements, collecting forces, flow fields and surface pressures, were performed using three tyre profiles and two rim configurations. A reference tyre was used to characterise the main flow mechanisms around the wheels and wheelhouses.

2. Methodology

2.1. Vehicle geometry

A full-scale, production-detail, electric, crossover SUV was tested in a closed cooling configuration, achieved by taping the front cooling inlets. The characteristic dimensions of the vehicle are given in Fig. A.1, Appendix A. The tyres were made with different shoulder and sidewall geometries, Fig. 2, but were otherwise identical. All tyres had the same fully detailed tread pattern. The nominal tyre size was 245/45R19 with a rim width of 7.5 inches. Two rim configurations were used, open and closed, where the latter was achieved by attaching a convex carbon fibre sheet to the outside surface of the rim (Fig. 3). Throughout this work, we will refer to wheel as being the combination of both tyre and rim. Although the frontal area changed slightly between the configurations, a constant value of 2.54 m^2 was used for calculating all force coefficients.

2.2. Wind tunnel

The test was performed in the Volvo Cars Aerodynamic Wind Tunnel (PVT). The wind tunnel has a slotted wall test section with a cross-sectional area of 27.1 m^2, resulting in a blockage of 9.4% with the current test object. PVT is equipped with a boundary layer control system consisting of a scoop, distributed suction and a five-belt moving ground system, as illustrated in Fig. 4. The five-belt system consists of a 1 m wide centre belt and four wheel drive units (WDUs), providing the wheel rotation. The exposed area of the WDU belts is tangential to the ground and measures 400 × 360 mm (length × width). The flat surface results in a realistic tyre contact patch. The belts are placed such that the contact patch is centred on them. Four rocker panel restraint posts with a diameter of 36 mm are used to fix the vehicle to the underfloor balance. The front right WDU belt and strut are visible in Fig. 3.

The wind tunnel follows the accreditation SS-EN ISO/IEC 17025:2018 (Swedac, 2020) and the uncertainty is regularly checked using a reference vehicle. More details about the wind tunnel are given in Sternéus et al. (2007) and Ljungskog et al. (2019b), where the latter includes a detailed investigation of the flow quality and its associated uncertainty.

The tests were performed at 100 km/h (27.78 m/s), corresponding to a Reynolds number of $Re_{\sqrt{A}} = 2.9 \times 10^6$ based on the square root of the frontal area.

2.3. Force measurements

All forces presented in this work were averaged for 40 s and measured towards a common baseline within each test occasion. Hence, the uncertainty due to the mounting in the wind tunnel was mitigated.

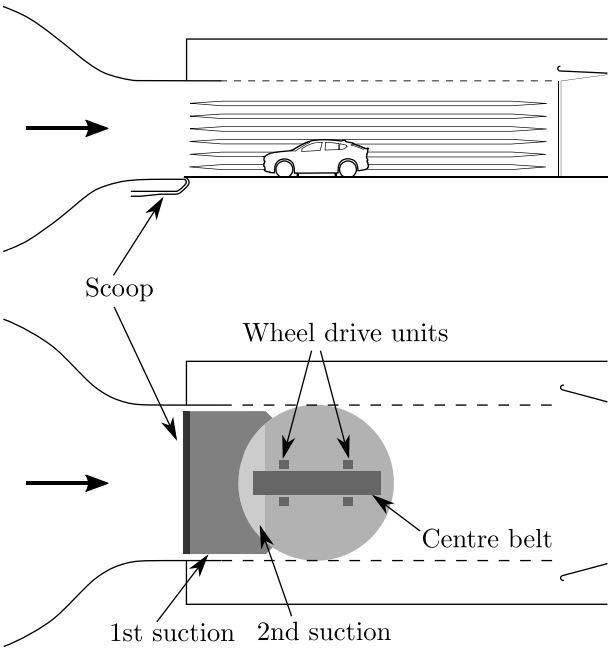

Fig. 4. Sketch of the test section and the boundary layer control system in PVT. *Source:* Adapted from Ljungskog et al. (2019a), drawn to scale.

Table 1
Force coefficient 95% uncertainty estimations. The base drag is calculated from the pressure measurements, as described in Section 2.4.

Force	Coefficient	Uncertainty
Drag	C_D	±0.0011
Front lift	C_{LF}	±0.0006
Rear lift	C_{LR}	±0.0013
Base drag	C_{DB}	±0.0013

To estimate the uncertainties of the force measurements, ten measurements of the same configuration were performed, resulting in the 95% confidence intervals presented in Table 1. Considering that the results will be later discussed in terms of force deltas towards the reference tyre, the uncertainties in Table 1 are combined using the root sum squared method, resulting in a scaling by $\sqrt{2}$.

2.4. Pressure measurements

Simultaneously with the force measurements, unsteady pressure measurements were performed in the right-hand side wheelhouses and at the vehicle base. Each wheelhouse was equipped with nine sensors along the cross-section $y = 750$ mm, approximately corresponding to the middle of the tyre. The sensors were placed circumferentially relative to the wheel axle with an even angular spacing of 22.5° (approximately 170 mm). At the right-hand side of the vehicle base, 29 spades were placed with a horizontal and vertical spacing of 150 and 160 mm, respectively.

First Sensor HCLA0025DB units with a range of ±2500 Pa were used. The sensors were statically calibrated to within ±5 Pa, corresponding to ±0.01 C_p at 100 km/h. The pressures were sampled at 5000 Hz for 60 s using two Dewesoft Sirius modules. The averaging time was found to result in a 95% uncertainty of less than ±0.002 and ±0.006 C_p for the mean pressure at all wheelhouse and base sensors, respectively.

The wheelhouse sensors were connected with 10 cm long tubes, allowing analysis of the transient signals without applying any transfer function. Using the method developed by Bergh and Tijdeman (1965) it was shown that negligible amplitude and phase shifts were obtained for frequencies below 100 Hz, which are the frequencies of interest for aerodynamic analysis. This was also confirmed by applying a low-pass filter to the signal, showing no discernible difference compared to the unfiltered signal.

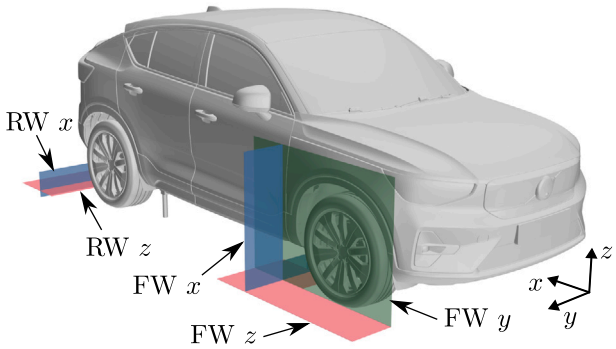

Fig. 5. Planes used for flow field measurements.

The base pressure sensors were connected with longer tubes, hence only the averaged values were considered. The base drag coefficient, C_{DB}, was calculated by integrating the pressure over the measurement area and multiplying by two to correspond to a full vehicle. This should be valid due to both the top-hat and underbody being largely symmetric, which was also confirmed by the base pressure in numerical simulations.

The measurements used the standard wind tunnel reference pressure, calculated as

$$P_\infty = P_{C2} + k_p \Delta P, \tag{1}$$

were P_{C2} is the pressure at the roof of the nozzle contraction, $k_p \approx 0.06$ is a calibration coefficient from the wind tunnel commissioning and ΔP is the pressure drop over the nozzle (approximately 460 Pa at 100 km/h).

For further insight into the propagation of fluid structures the cross-correlation between the wheelhouse sensors, defined as

$$C^{\text{norm}}_{X,Y}(\tau) = \frac{\text{Cov}\left[X(t), Y(t+\tau)\right]}{\sqrt{\text{Var}\left[X(t)\right]\text{Var}\left[Y(t)\right]}}, \tag{2}$$

was investigated. Both the case with and without lag was considered. The case without lag, $C^{\text{norm}}_{X,Y}(\tau = 0)$, will be referred to as correlation, whereas the general case is denoted cross-correlation.

2.5. Flow field measurements

Flow field measurements were taken using two twelve-hole Omniprobes and the traversing gear of the wind tunnel. Fig. 5 shows the investigated planes. FW and RW denote front and rear wheel, respectively. FW x was located 500 mm downstream of the front wheel axle, FW y was 25 mm outside of the tyre bulge and FW z was taken 25 mm above the ground. At the rear wheel, RW x was taken 500 mm behind the rear wheel axle and, to avoid measuring mostly the boundary layer built up along the wind tunnel floor, RW z was taken 80 mm above the ground.

Sampling the twelve pressures on each probe, the manufacturers' calibration can be used to calculate the static and dynamic pressure as well as the three velocity components. The probes measure the flow within ±150° and, to better capture the reversed flow in wakes, the probes were placed at 45° relative to the freestream direction. The accuracy of the probes is reported to be within 3% for the velocity magnitude and ±1.5° for the flow angle (Aeroprobe corporation, 2015). The two probes were placed with a vertical spacing of 56 mm.

The Γ_2 variable, proposed by Graftieaux et al. (2001), was employed to visualise vortices. This variable is less sensitive to noise compared to, for example, vorticity or the Q-criteria, which both require differentiation (De Gregorio and Visingardi, 2020). It should be noted that Γ_2 only

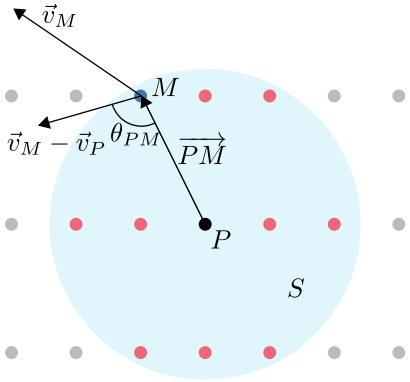

Fig. 6. Illustration of the calculation of Γ_2 around a point P in region S. The size of S in relation to the spacing between the measurement points is not to scale. Inspired by Parfett et al. (2022).

indicates the position and size of the vortices and not their strengths. The degree of rotation is determined by first constructing the average velocity $\vec{v}_P$ in a region S around the studied point P as

$$\vec{v}_P = \frac{1}{N} \sum_{M \in S} \vec{v}_M. \tag{3}$$

Γ_2 is then calculated as

$$\begin{aligned} \Gamma_2 &= \frac{1}{N} \sum_{M \in S} \frac{\left[\overrightarrow{PM} \times \left(\vec{v}_M - \vec{v}_P\right)\right] \cdot \hat{n}}{\|\overrightarrow{PM}\| \cdot \|\vec{v}_M - \vec{v}_P\|} \\ &= \frac{1}{N} \sum_{M \in S} \sin\theta_{PM}, \end{aligned} \tag{4}$$

where $\hat{n}$ is the plane normal and M denotes the other points in S. Γ_2 can be illustrated as the mean angle between $\overrightarrow{PM}$ and $\vec{v}_M - \vec{v}_P$, Fig. 6. The size of S regulates the amount of resolution compared to spatial averaging. Here, a disk with radius 50 mm was found to be suitable.

The data was recorded continuously at 20 Hz while sweeping the probes at a velocity of 40 mm/s along lines spaced 28 mm apart. The data was time-averaged by calculating an average along 10 mm of travel, corresponding to approximately 0.25 s averaging time. Compared to the traditional approach of sampling the pressures with the probe stationary in discrete points, this method significantly reduces the time required for measurements. To investigate the repeatability of the method, especially in terms of time-averaging of the unsteady flow, ten identical measurements were performed in the lower part of the FW x plane. Fig. 7 shows the average total pressure coefficient and Γ_2 along with the isolines from the ten measurements at $C_{ptot} = 0$ and $|\Gamma_2| = 0.4$ (arbitrarily chosen to illustrate the repeatability). They all result in similar isolines, indicating that the repeatability of the method is sufficient for analysing differences between tyres.

The measurements with the traverse are known to be intrusive, altering the flow and vehicle forces (Sterken et al., 2014). However, previous investigations, using the same wind tunnel and equipment, have shown that the flow structures are still qualitatively similar (Sterken et al., 2014; Josefsson, 2022).

3. Results

This section starts with presenting the global force differences for the three tyres and the two rims compared to the reference tyre. Then, the flow field measurements are considered. The analysis is first performed for the closed rim. Later, the differences with the open rim are highlighted. Lastly, the surface pressure measurements in the wheelhouses and at the vehicle base are analysed to further characterise the flow.

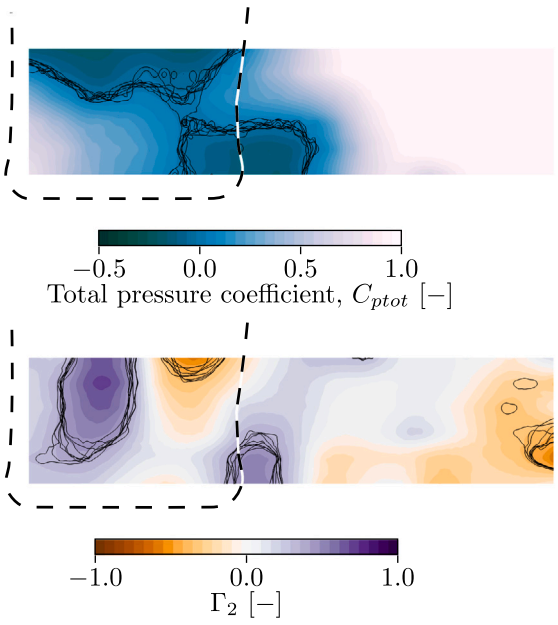

Fig. 7. Mean field and isolines from ten repeated measurements in the lower part of the FW x plane. The isolines are drawn at $C_{ptot} = 0$ and $|\Gamma_2| = 0.4$. The dashed line marks the outline of the wheel. Positive Γ_2 corresponds to a counterclockwise rotation.

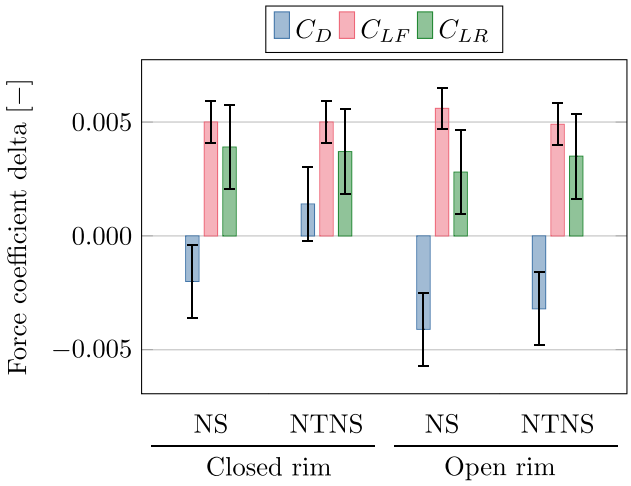

Fig. 8. Force coefficient deltas relative to the reference (R) for the two rims. The error bars correspond to $\sqrt{2}$ of the values given in Table 1.

3.1. Force coefficient deltas

Fig. 8 shows the drag, front lift and rear lift (C_D, C_{LF}, C_{LR}) deltas compared to the reference tyre for the two rims. With the closed rim, a slight drag decrease is observed with the narrow sidewall (NS) whereas a small drag increase is obtained with the narrow tread and narrow sidewall (NTNS). For the open rim, both tyres reduce the drag by $0.003-0.004\ C_D$. More consistent results are observed for the lift forces, with similar increases of both front and rear lift for all cases.

3.2. Closed rim

3.2.1. Reference tyre (R)

Fig. 9(a) shows the flow field of the reference tyre at the front right wheel. As visible in the FW z plane, the oncoming flow is yawed, creating an angled wake. A distinct outer contact patch separation is seen in

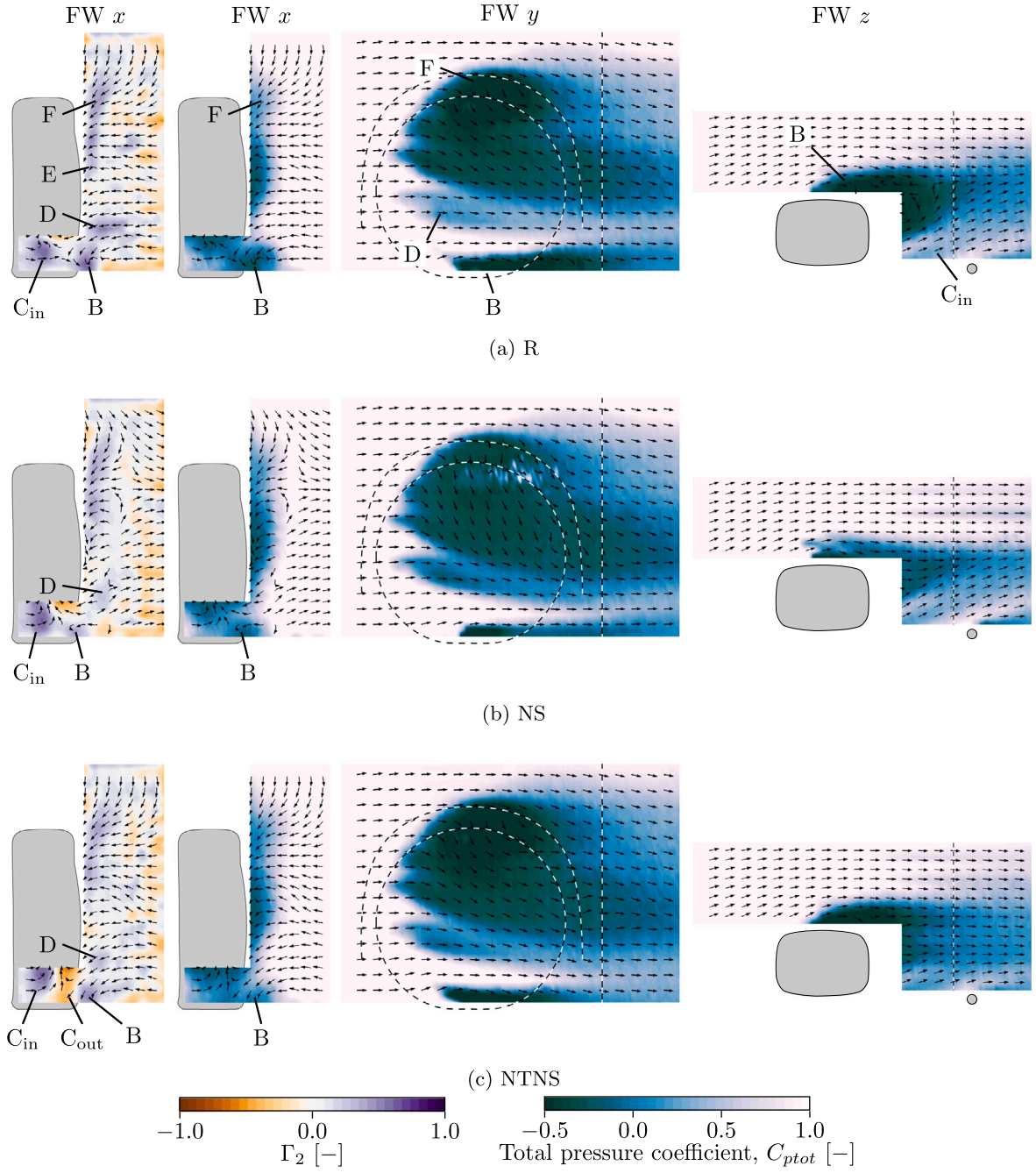

Fig. 9. Flow field measurements at the front right wheel with the closed rim and the three tyre profiles. The displayed quantities are, from left to right, Γ_2 in FW x followed by C_{ptot} in FW x, FW y and FW z. The dashed lines mark the position of the wheel, wheelhouse and FW x plane. In FW z, the location of the mounting strut is indicated.

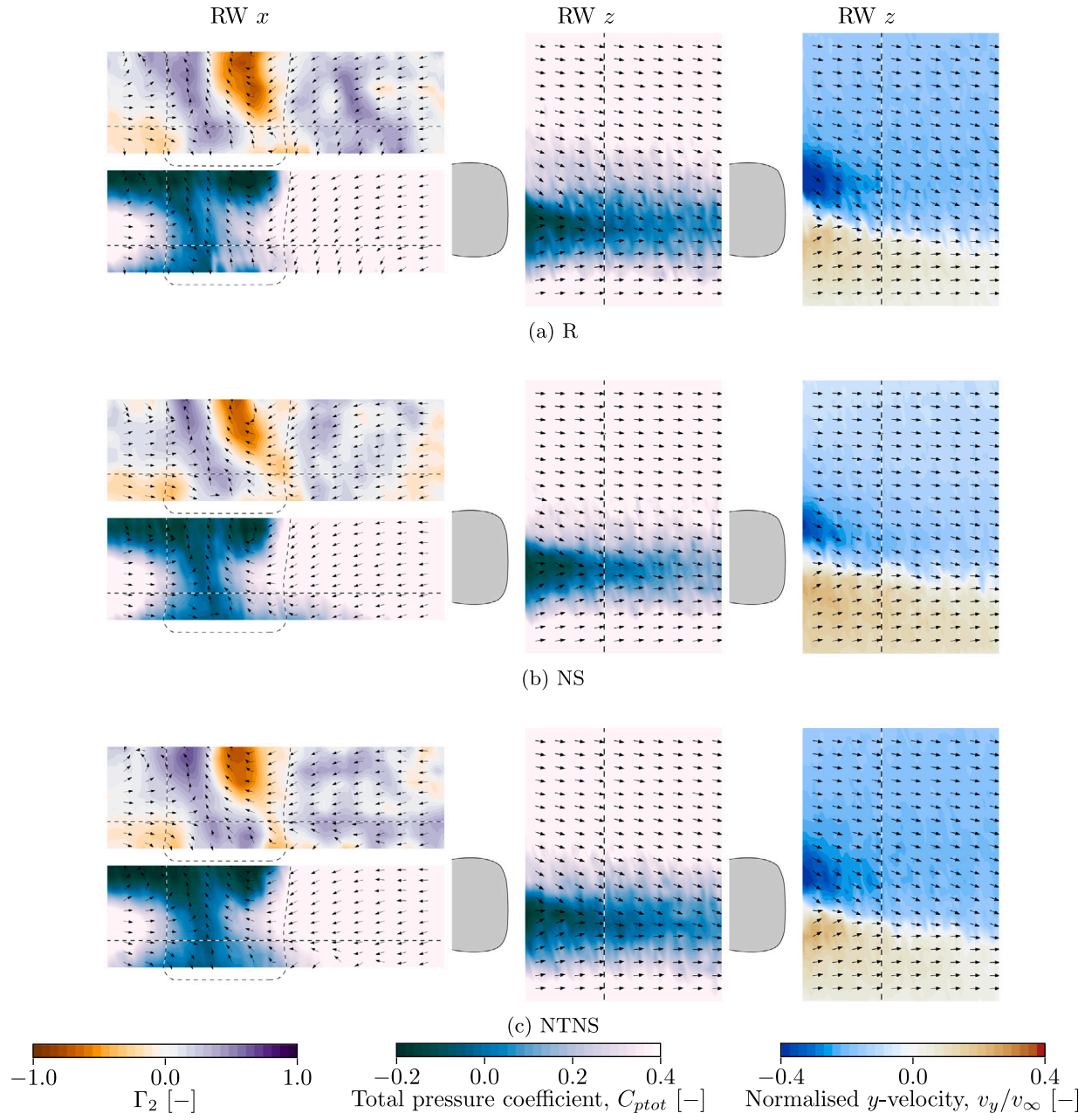

Fig. 10. Flow field measurements at the rear right wheel with the closed rim and the three tyre profiles. The displayed quantities are, from left to right, Γ_2 and C_{ptot} in RW x followed by C_{ptot} and v_y/v_∞ in RW z. The dashed lines mark the outline of the tyre, RW z and RW x.

all planes. The low-energy region corresponds to the counterclockwise rotating (positive Γ_2) outer contact patch vortex (B according to Fig. 1). Further inside in the Γ_2 plot, the inner part of vortex pair C is seen. The outer part of C is not seen for this configuration in this plane. With these two counterclockwise rotating vortices there is a strong outflow, as visible in FW z.

Above the outer contact patch vortex there is another region of positive Γ_2. Comparing to FW y, this corresponds to the faint low-energy region found slightly below the wheel centre. This is believed to correspond to the lower part of D. The strength of D is largely determined by the rim flow (Wäschle, 2007). Hence, it is expected to be weak for a closed rim. Comparing to a similar investigation using the DrivAer (Josefsson et al., 2022), this vortex was only observed for an open rim. A probable reason for the vortex being visible here is that convex rim covers were used, pushing the structure slightly outwards, into the measurement plane.

Above D a large separated region is observed in FW y. Inside the separation, a downwash is obtained. From Γ_2, a vortex coinciding with the lower part of E is seen slightly above the wheel centre. Above this, the wheelhouse vortex F is found. The clockwise rotating upper part of E is not observed since it is believed to be located closer to the tyre.

Overall, the vortex structure is similar to the one observed by Wäschle (2007). The only major deviation is the lack of vortex A in the measurements, which could be explained either by that it is not prominent for this wheel-vehicle combination or that it is outside of the measured planes.

Fig. 10(a) shows the flow field in the two rear wheel planes. As illustrated by the total pressure in RW z, the wake is shifted towards the inner side of the tyre (bottom of the figure). This is also illustrated by the strong inflow downstream of the outer tyre shoulder, as shown by the region of negative spanwise velocity. The inwards positioning of the wake is also visible in FW x, where the arrows indicate that the inflow from both tyre shoulders results in an upwash downstream of the tyre. From Γ_2, a pair of counter-rotating vortices is observed. The outer vortex (negative Γ_2) is more prominent, likely due to the strong inflow at the outer tyre shoulder.

3.2.2. Narrow sidewall (NS)

Fig. 9(b) shows the flow field with the narrow sidewall tyre. Before analysing the results it should be noted that the vectors in the outer part of FW x indicate an outwards flow, opposite to the reference. The difference is however very small since the vectors do not reflect the size of the in-plane velocity but only its direction. The analysis of the flow fields will refer to Γ_2 and C_{ptot} in Fig. 9. To highlight the differences, Fig. B.1 in Appendix B, displaying ΔC_{ptot}, is provided.

Comparing Γ_2 to the reference, the outer contact patch vortex (B) is smaller and located closer to the tyre. The difference can be observed already upstream of the wheel centreline in FW z, indicating that it comes from the front tyre shoulder. With the reduced vortex, a smaller wake is formed further downstream. The outwash is slightly weaker and, instead, there is more upwash downstream of the tyre, as visible in FW x. The upwash makes more flow enter the rear part of the wheelhouse, increasing the leakage from the wheelhouse top and resulting in a larger low-energy region in the top part of FW x. This upwash was also observed in the FW z plane, although not shown here. The low-energy region corresponding to the lower part of vortex D, is more distinct in the upstream parts of FW y, indicating that the narrow sidewall exposes the rim flange more than the reference.

At the rear wheel, Fig. 10(b), there are only minor differences compared to the reference. There is a slight reduction of the inflow at the outer tyre shoulder, as illustrated by the spanwise velocity. With this, the outer vortex is smaller.

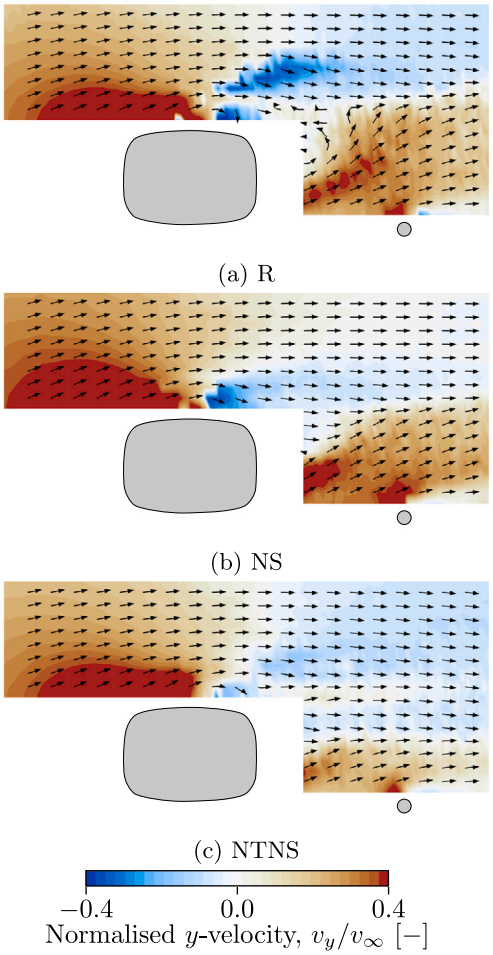

Fig. 11. Normalised spanwise velocity in the plane FW z for the closed rim.

3.2.3. Narrow tread and narrow sidewall (NTNS)

With the narrow tread and narrow sidewall the drag is slightly larger than for the reference tyre, Fig. 8. The outer contact patch vortex (B) is larger and placed further outwards compared to NS, Fig. 9(c) FW x. Slight differences can be observed already far upstream in FW z, indicating that it is caused by the shoulder curvature. Similarly to NS, a more distinct lower part of D is obtained.

The outer, clockwise rotating, part of vortex pair C is now visible in the Γ_2 plot. It is created by the separation at the downstream tyre shoulder. With the round shoulder of NTNS, a stronger inflow is likely obtained, producing a stronger outer C vortex. This increases the upwash in the wake, resulting in more flow entering the wheelhouse and a larger upper separation. Comparing the total pressure in FW z to R, the effect on the overall wake direction can be seen with a more straight wake for NTNS. This is further illustrated by the spanwise velocity, Fig. 11. R and NS both result in a strong outwash from the inner tyre shoulder (bottom of the figures) which then is counteracted by inflow from the tyre outside. With NTNS, the outwash is less and an area of negative y-velocity can be seen behind the tyre, caused by C outer.

At the rear wheel, Fig. 10(c), the flow is very similar to the reference.

3.3. Open rim

3.3.1. Reference tyre (R)

With the open rim, drag increases by 0.012 C_D. The same overall flow mechanisms as described for the closed rim are still observed,

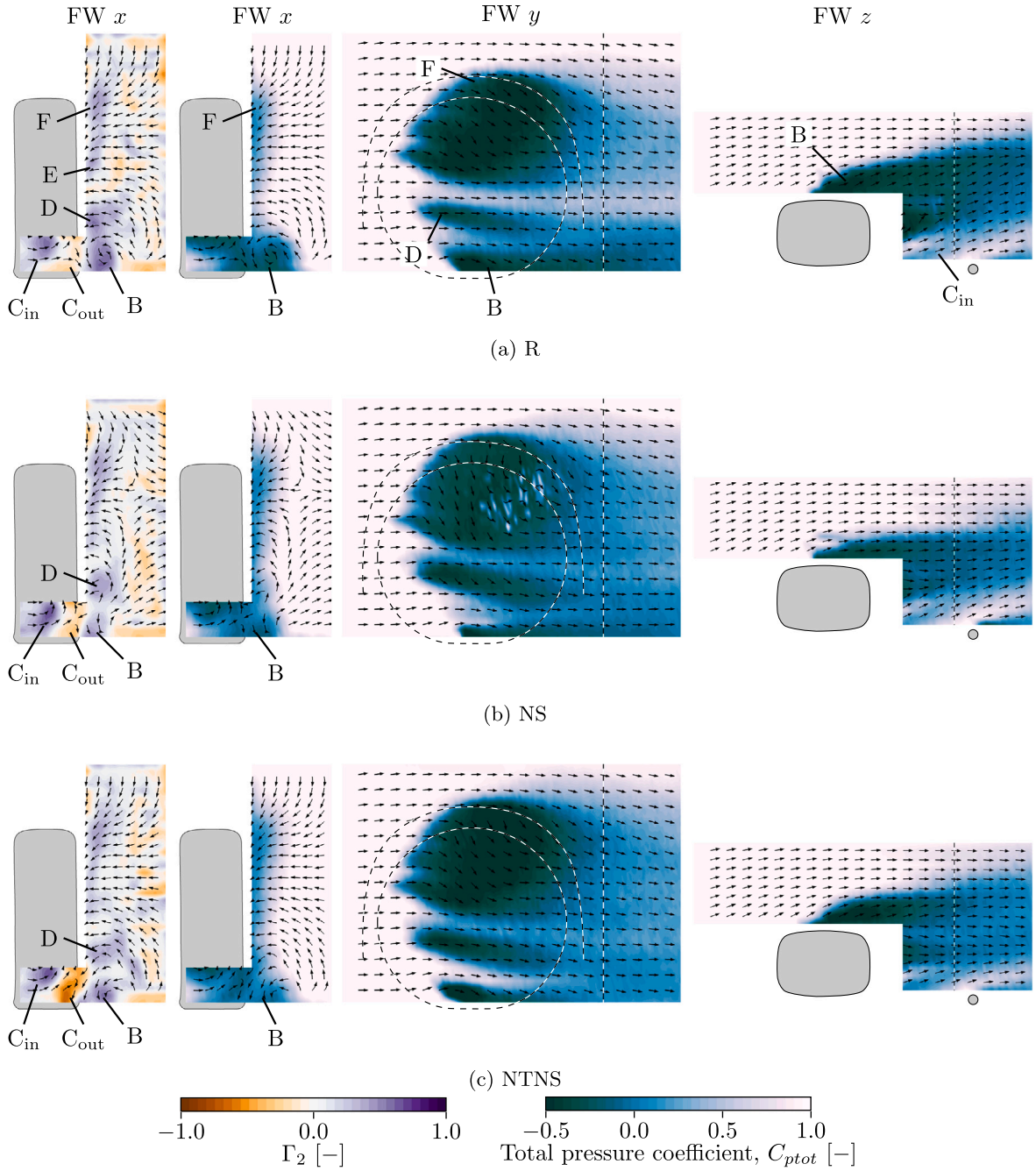

Fig. 12. Flow field measurements at the front right wheel with the open rim and the three tyre profiles. The displayed quantities are, from left to right, Γ_2 in FW x followed by C_{ptot} in FW x, FW y and FW z. The dashed lines mark the position of the wheel, wheelhouse and FW x plane. In FW z, the location of the mounting strut is indicated.

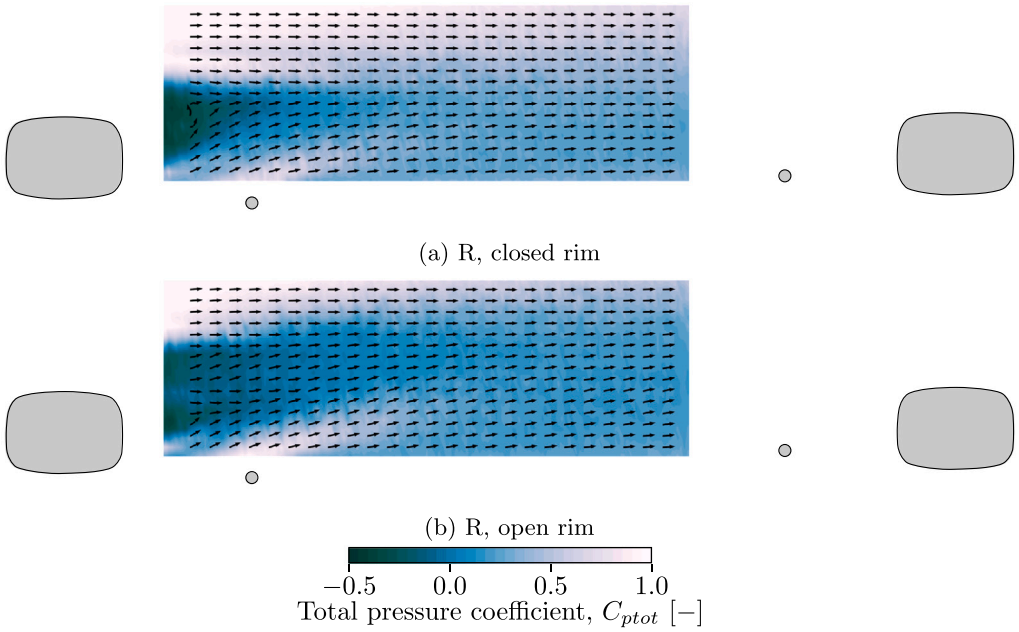

Fig. 13. Total pressure coefficient in an extended FW z plane showing the direction of the wheel wake for the closed and open rims with the reference tyre.

but their relative importance is altered. Fig. 12(a) shows the flow field measurements at the front right wheel (for delta plots between open and closed rims, see Appendix B, Fig. B.3). The contact patch vortex (B) is larger, as seen in all planes, resulting in a larger wake that extends both further downstream and outwards. This is further established by considering an extended FW z plane, Fig. 13. The open rim not only results in a larger low-energy region, but also more outwash far away from the front wheel.

Returning to Fig. 12(a), a more distinct lower D vortex is measured in FW x and FW y. This confirms that it is dependent on the rim geometry, as theorised by Wäschle (2007). In FW x, B and D have almost merged, as indicated by Γ_2.

The low-energy region created from the upper half of the wheel does not extend as far downstream with the open rim as with the closed rim, as observed in FW x and y. This is believed to be caused by the convex rim covers. With the open rim, the outer part of vortex pair C becomes more visible. This is explained by the contact patch vortex being further outwards, allowing C outer to be seen in the FW x plane. Overall, the differences between open and closed rims agree well with previous research (Hirose et al., 2019; Brandt et al., 2019; Josefsson et al., 2022).

Fig. 14(a) shows the flow at the rear wheel. Compared to the closed rim (Fig. 10(a)), the region of negative spanwise velocity is bigger. With the open rim, the counterclockwise rotating vortex is larger and closer to the ground, intersecting the RW z plane and potentially explaining why the inflow is stronger there. Far outside of the tyre, a faint region of low-energy flow is visible, likely originating from the front wheel. Such a region was not seen for the closed rim, again illustrating the more outwashed front wheel wakes.

3.3.2. Narrow sidewall (NS)

Compared to the closed rim, a larger drag reduction is obtained with NS on the open rim, Fig. 8. As for the closed rim, a reduced outer contact patch separation (B) is observed in all planes, Fig. 12(b) (see Fig. B.2 for ΔC_{ptot}). This reduces the outwash seen outside of the tyre in FW z. The high energy outflow from the inner tyre shoulder remains. There is more inflow into the rear of the wheelhouse, resulting in a larger upper separation, as seen in FW x. Overall, the changes are very similar to the closed rim. Hence, the drag reduction of 0.004 C_D is likely explained by other mechanisms.

Fig. 14 shows the flow in the planes at the rear wheel. With NS, the strong inflow downstream of R reduces, as shown by the spanwise velocity in RW z and total pressure in RW x. This increase can be connected to a stronger clockwise rotating vortex seen in RW x. This effect was much smaller with NS on the closed rim, hence it is likely caused by the interaction between the tyre and the rim and the difference in wake direction that was observed in Fig. 13. With the narrow sidewall, the outwash at the front wheel is altered, changing the interaction between the front wheel wake and the rear wheel, resulting in a more balanced rear wheel wake.

3.3.3. Narrow tread and narrow sidewall (NTNS)

Similar to the closed rim, the contact patch vortex (B) is larger than for NS and there is a distinct C_{out} vortex, Fig. 12(c). The outwash downstream of the front wheel is reduced compared to R (FW x and FW z). More upwash and a larger upper separation are seen in FW x. The altered front wheel wake improves the flow at the rear wheel, creating a more symmetric wake, Fig. 14(c).

3.4. Surface pressure measurements

Unsteady pressure measurements were taken in the wheelhouse to help the characterisation of the flow around the wheels, while time-averaged base pressures were considered to connect the local flow changes to the vehicle drag.

3.4.1. Wheelhouse pressures

Front wheelhouse flow To understand the flow mechanisms in the wheelhouse, where the traverse cannot be used, the wheelhouse surface pressures were measured. Only small differences were observed

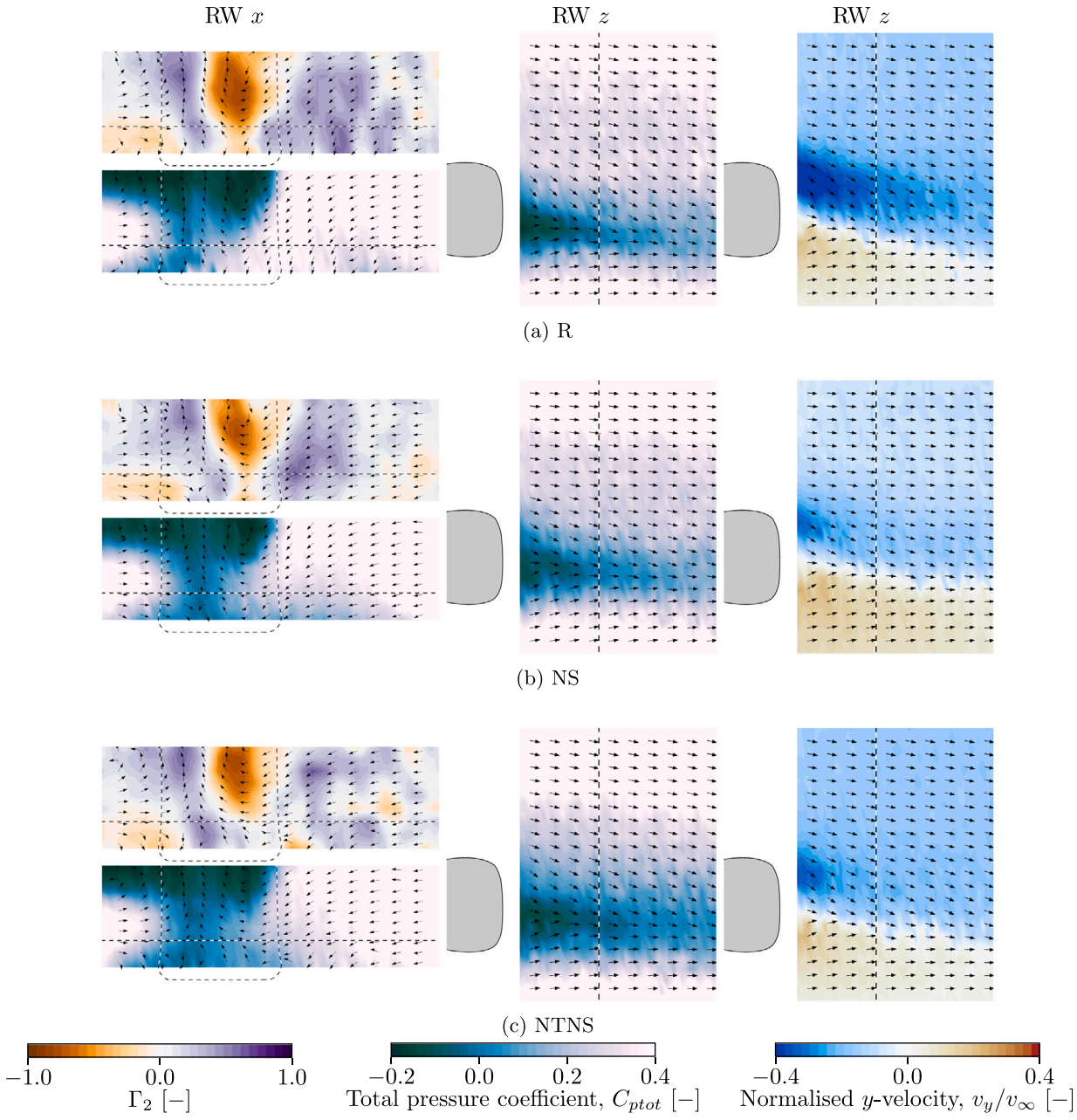

Fig. 14. Flow field measurements at the rear right wheel with the open rim and the three tyre profiles. The displayed quantities are, from left to right, Γ_2 and C_{ptot} in RW x followed by C_{ptot} and v_y/v_∞ in RW z. The dashed lines mark the position of the tyre, RW z and RW x.

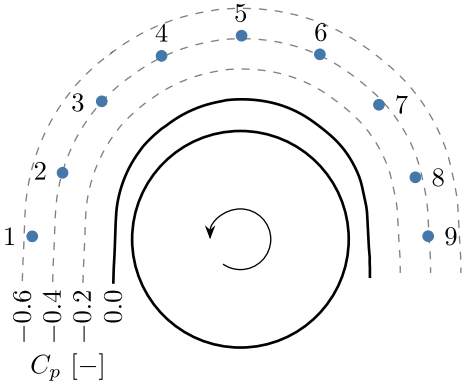

(a) Average pressure coefficient at front wheel. Flow from left to right. The integers (1-9) indicate the sensor names.

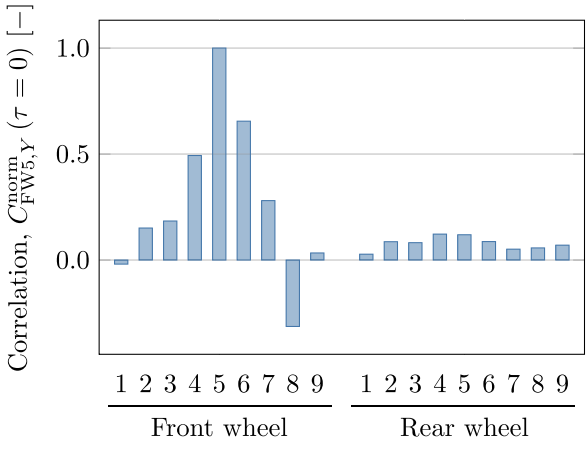

(b) Correlation between wheelhouse sensors and sensor 5 at the front wheel.

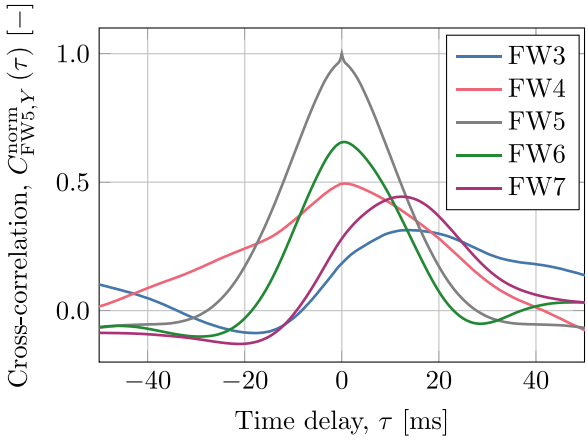

(c) Cross-correlation to sensor 5 at the front wheel as a function of the time delay, τ.

Fig. 15. Pressure measurements in the front right wheelhouse with correlation to front wheel sensors 5 (FW5).

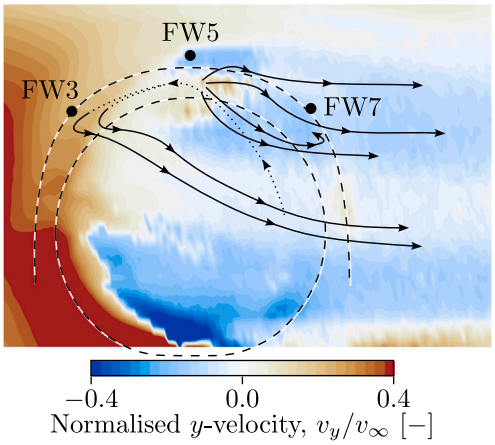

Fig. 16. Normalised spanwise velocity in the FW y plane with a schematic illustration of the flow between pressure sensors 3, 5 and 7. Dotted lines represent the flow inside the wheelhouse, behind the wheel. Positive y-velocity corresponds to flow out from the vehicle. The dashed lines show the outline of the wheel and outer wheelhouse edge.

between the different tyres and rims, hence mainly the reference tyre with the closed rim will be discussed. Fig. 15(a) shows the mean pressures in the front right wheelhouse. Overall, a homogeneous pressure distribution is obtained with $C_p \approx -0.4$ along the measured cross-section.

Fig. 15(b) shows the correlation between front wheel sensor 5 (located at the top of the wheelhouse, Fig. 15(a)) and all other wheelhouse sensors. The highest correlation of sensor 5 occurs for the neighbouring sensors 4 and 6. Investigating the correlation as a function of the time delay, information about the propagation of structures can be obtained (Bonitz et al., 2018), Fig. 15(c). Sensors 4 and 6 show no time delay, indicating that one coherent structure spans all sensors. Sensors 3 and 7 have the highest correlation for a time delay of $\tau \approx 12$ ms, indicating that the structures propagate from 5 to both 3 and 7. Combining the cross-correlation with the y-component of the velocity in FW y and with the help of smoke visualisation performed during the tests and a high-fidelity CFD simulation, a schematic illustration is created, Fig. 16. The flow reaching the top of the wheelhouse mainly flows inside of the measured cross-section, reaching sensor 5 first. The flow around sensor 5 then continues forward, towards sensor 3, or exits the wheelhouse, contributing to the large upper separation. Some of the exiting flow re-enters at the downstream wheelhouse arch, resulting in the correlation between 5 and 7.

Rear wheelhouse flow Fig. 17(a) shows the mean pressure coefficient at the probes in the rear wheelhouse. Similar to the front wheel, a rather homogeneous pressure is obtained in the entire cross-section, with $C_p \approx -0.2$. The correlation to sensor 5 is large for most other sensors in the rear wheelhouse, indicating more flow in the plane of the sensors than for the front wheel, Fig. 17(b). Including the time delay, it is found that the flow propagates from the front towards the rear of the wheelhouse, Fig. 17(c). A weak, but clear, cross-correlation to the front wheel sensors is also found, here illustrated by FW7. The time delay of approximately 100 ms is expected given the wheelbase of 2702 mm and freestream velocity of 27.78 m/s, corresponding to 97 ms. This demonstrates that there is an interaction between the front wheel wakes and the rear wheels to such an extent that it is measurable by the rear wheelhouse sensors.

The connection between the front wheel wakes and the rear wheels can be further established by comparing the cross-correlation for all tyres and rims, Fig. 18. Generally, the differences between the tyres are small. There is, however, a clear trend between the two rims. The physical reason for this difference cannot be explained with certainty from the available data. However, it illustrates that the interaction

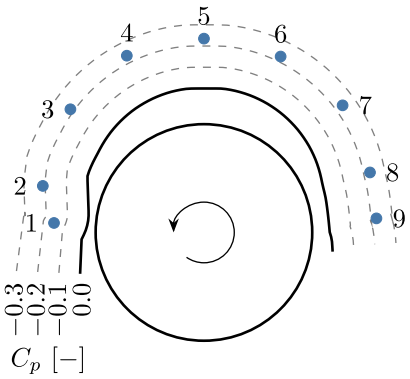

(a) Average pressure coefficient at rear wheel. Flow from left to right. The integers (1-9) indicate the sensor names.

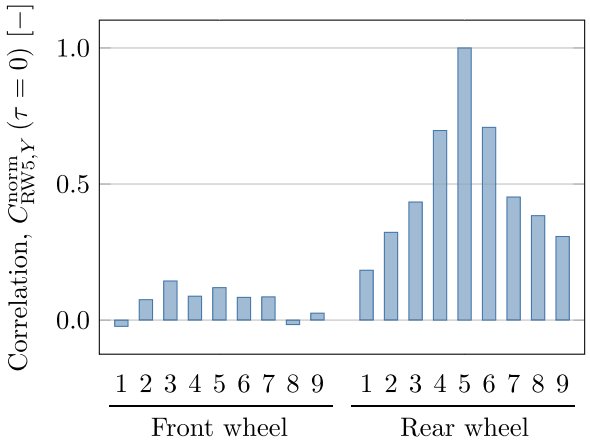

(b) Correlation between wheelhouse sensors and sensor 5 at the rear wheel.

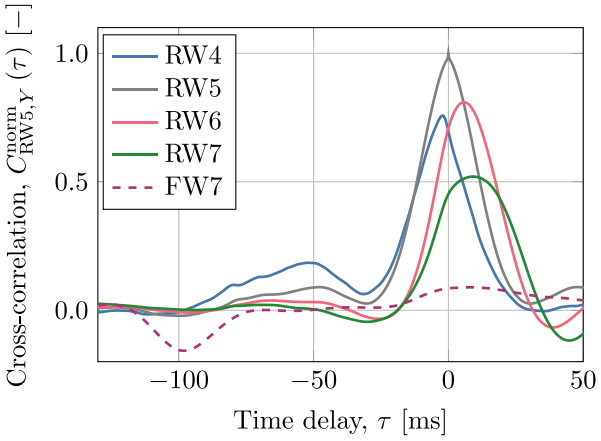

(c) Cross-correlation to sensor 5 at the rear wheel as a function of the time delay, τ.

Fig. 17. Pressure measurements in the rear right wheelhouse with correlation to rear wheel sensors 5 (RW5).

between the front wheel wake and the rear wheel can be modified, as discussed in connection to Fig. 13.

3.4.2. Base pressures

Here, the drag coefficient measured by the wind tunnel balance is compared to the base drag coefficient calculated from the base pressure

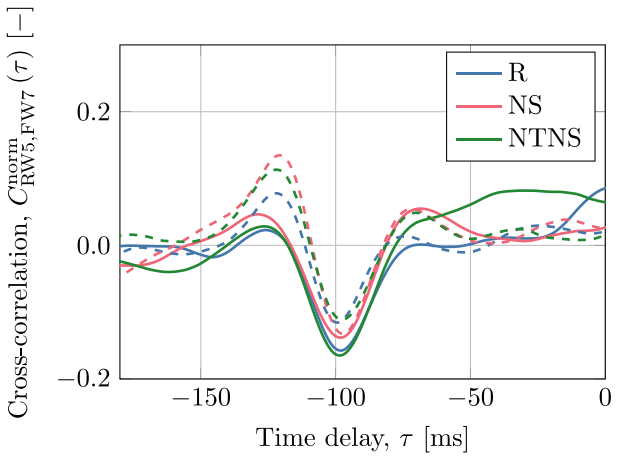

Fig. 18. Cross-correlation between rear wheel sensor 5 and front wheel sensor 7 for all tyres and rims. The solid and dashed lines represent the closed and open rims, respectively. Note the difference in scale compared to Fig. 17(c).

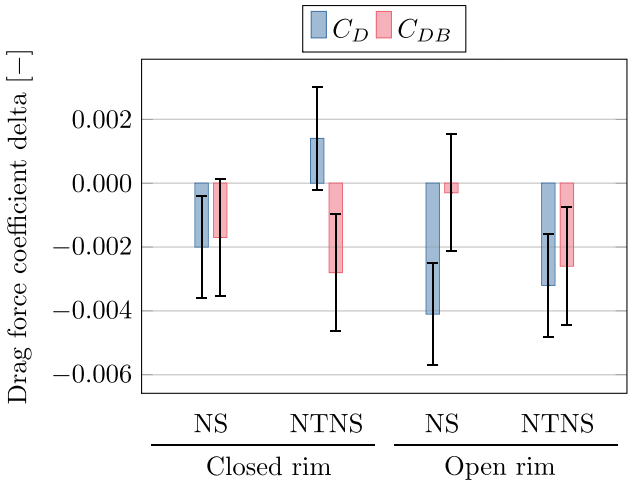

Fig. 19. Drag force coefficient deltas relative to the reference (R) with the two rims for the entire vehicle, C_D, compared to base drag, C_{DB}. The error bars correspond to $\sqrt{2}$ of the values given in Table 1.

measurements, Fig. 19. As can be seen, there is no clear connection between the overall drag and the base drag.

Fig. 20 shows the base pressure of R compared to NS and NTNS with the closed rim. Both NS and NTNS result in a pressure increase in the bottom right corner of the base, indicating an effect from the differences in the wheel wakes. For NS, the benefit is partly mitigated by a slight pressure reduction at the centre of the base. Similar differences between the tyres are observed with the open rim (not shown here).

Combining all results, it is believed that the drag reduction with the NS tyre is connected to the smaller contact patch separation at the front wheel. With the NTNS tyre, the effect of the reduced contact patch vortex is counteracted by a more prominent C_{out} vortex. Given the base drag reduction and the similar changes to NS at the rear wheel, there is likely an overall drag penalty at the front wheel for NTNS. With the open rim, the larger drag reduction is due to the altered interaction between the front wheel wake and the rear wheel.

4. Conclusions

Three tyre profiles were investigated using full-scale wind tunnel measurements. Capturing forces, flow fields and unsteady surface pressures, the dominant flow mechanisms of the wheel wakes could

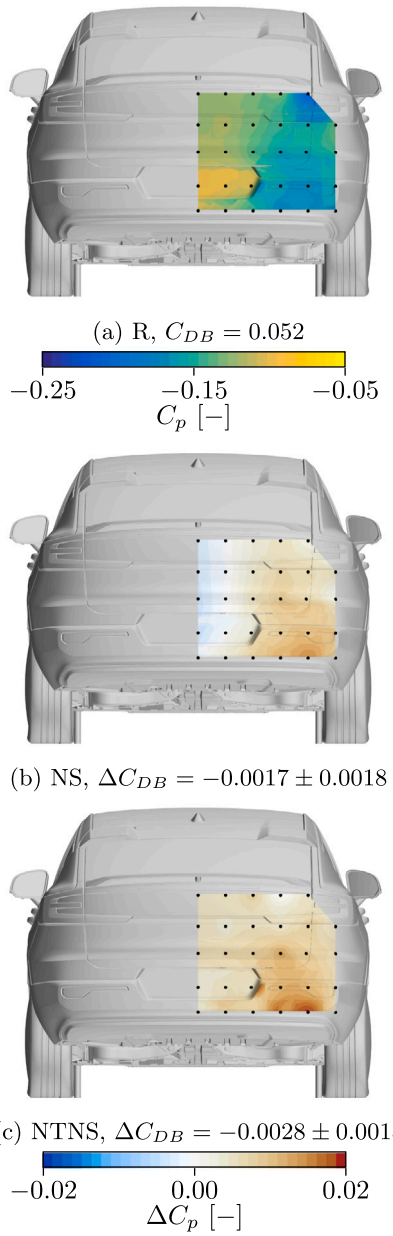

Fig. 20. Base pressure for R and corresponding deltas for NS and NTNS with the closed rim. The base drag, C_{DB}, corresponds to a full vehicle.

be identified. Initially, the flow field around the reference tyre with the closed rim was considered. The flow was characterised by the yaw angle created by the vehicle body, directing the wake outwards. The main vortices and how they affect the flow were identified and discussed. Using the unsteady wheelhouse pressure measurements, it was shown how the leakages from the top of the wheelhouse contribute to the external flow patterns.

Altering the tyre profile resulted in flow differences close to the ground, where the tyre is exposed to the high-energy flow outside of the wheelhouse. The drag was reduced with a narrower sidewall (NS), mainly due to a smaller contact patch separation. With a narrow tread and narrow sidewall, the drag increased compared to the NS case. Its more rounded shoulder geometry resulted in a larger contact patch separation and a more distinct vortex at the outer downstream shoulder which increased the flow into the wheelhouse. These results demonstrate that the flow is sensitive to the positioning of the transition between tread and sidewall and that larger shoulder curvatures are not always beneficial.

Comparing two rim configurations, the same flow mechanisms were observed but their relative importance was altered, mainly in terms of a larger contact patch vortex and a more outwashed front wheel wake with the open rim. Varying the tyres on the open rim resulted in larger drag deltas than for the closed rim. This was explained by how the difference in front wheel wake outwash affected the shielding of the rear wheels.

CRediT authorship contribution statement

Erik Josefsson: Conceptualization, Methodology, Software, Validation, Formal analysis, Investigation, Data curation, Writing – original draft, Visualization. **Simone Sebben:** Conceptualization, Methodology, Resources, Writing – review & editing, Supervision, Funding acquisition. **Magnus Urquhart:** Conceptualization, Methodology, Resources, Writing – review & editing, Supervision, Project administration, Funding acquisition.

Declaration of competing interest

The authors declare that they have no known competing financial interests or personal relationships that could have appeared to influence the work reported in this paper.

Data availability

The authors do not have permission to share data.

Acknowledgements

The authors would like to thank Pirelli for the collaboration where they produced the prototype tyres and shared their expertise. In particular, Dr. Luca Camosi (Pirelli) and PhD candidate Fabio Semeraro (Politecnico di Milano) are acknowledged for their contributions to the project.

Numerical simulations, performed during the pre-study, were enabled by resources provided by the Swedish National Infrastructure for Computing (SNIC), partially funded by the Swedish Research Council through grant agreement no. 2018-05973.

Funding

This work is funded by the Swedish Energy Agency, Sweden grant number P49114-1.

Appendix A. Vehicle measurements

See Fig. A.1.

Appendix B. Total pressure difference plots

Figs. B.1 and B.2 show ΔC_{ptot} relative to the reference tyre, R, for closed and open rims, respectively. Fig. B.3 shows ΔC_{ptot} between open and closed rims with tyre R.

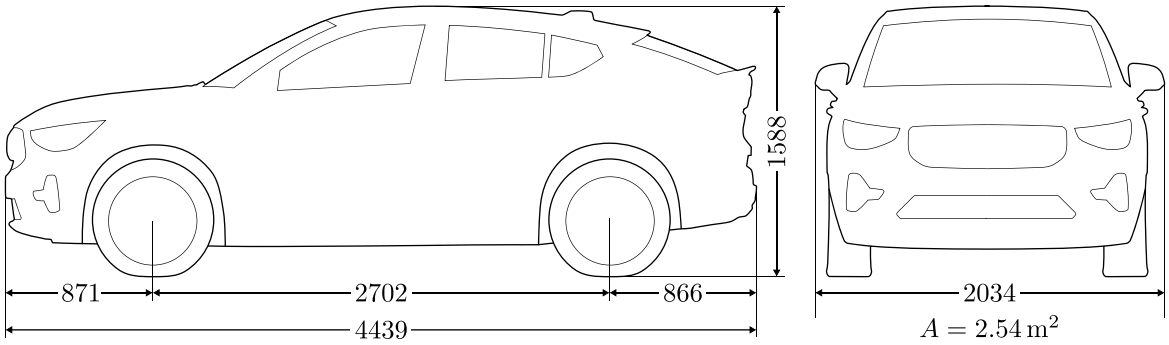

Fig. A.1. Characteristic measurements of the vehicle. All lengths are given in millimetres. A refers to the frontal area.

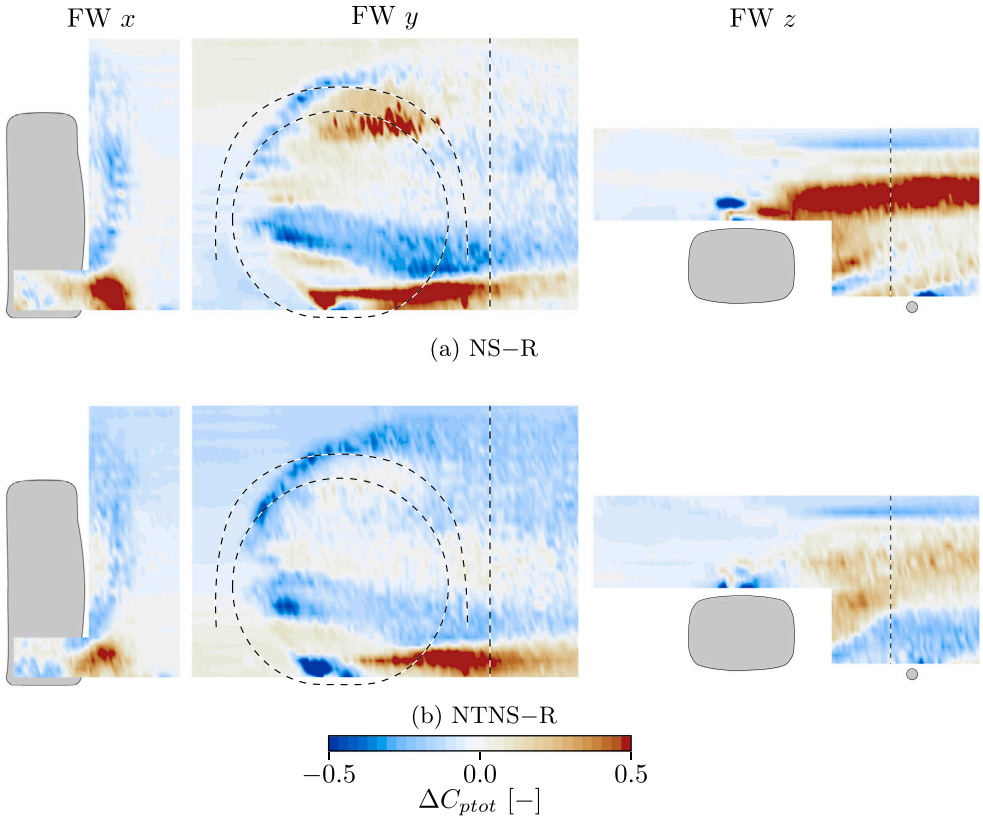

Fig. B.1. Difference in total pressure coefficient relative to tyre R with the closed rim. The dashed lines mark the position of the wheel, wheelhouse and FW x plane. In FW z, the location of the mounting strut is indicated.

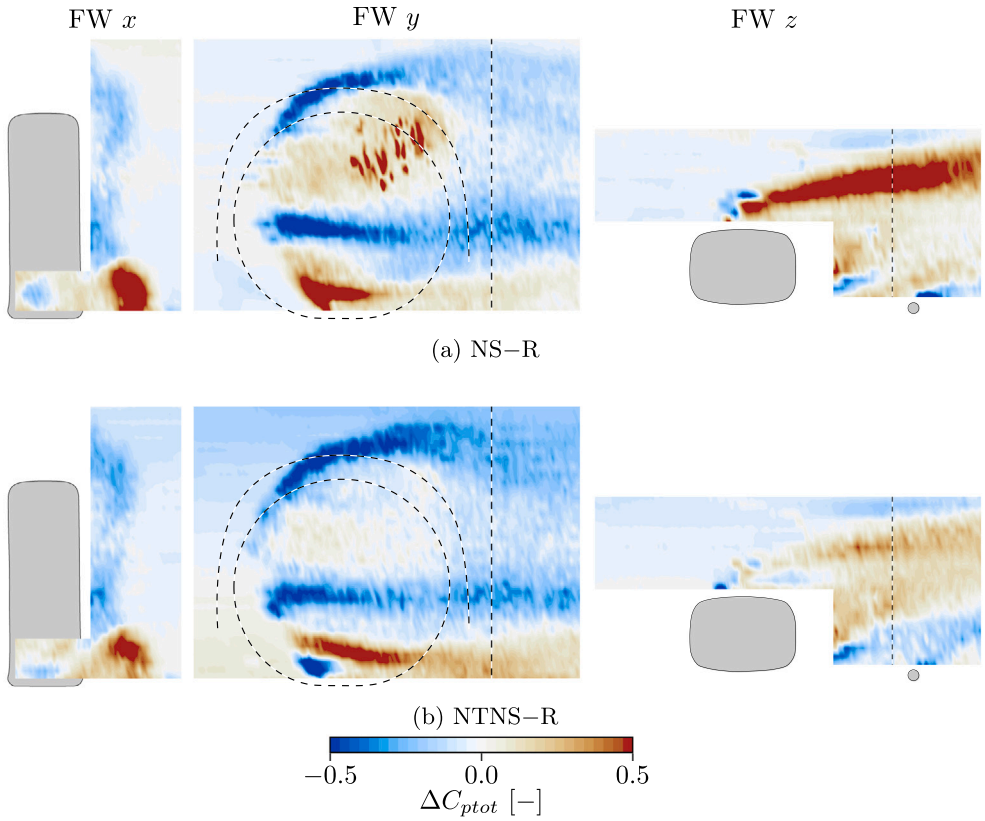

Fig. B.2. Difference in total pressure coefficient relative to tyre R with the open rim. The dashed lines mark the position of the wheel, wheelhouse and FW x plane. In FW z, the location of the mounting strut is indicated.

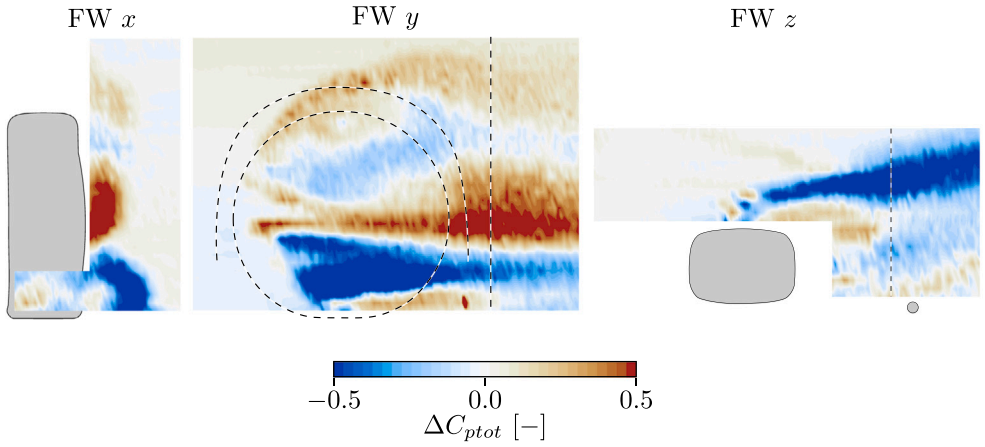

Fig. B.3. Difference in total pressure coefficient between the open and closed rims with tyre R. The dashed lines mark the position of the wheel, wheelhouse and FW x plane. In FW z, the location of the mounting strut is indicated.

References

Aeroprobe corporation, 2015. Standard probes user manual.

Bergh, H., Tijdeman, H., 1965. Theoretical and Experimental Results for the Dynamic Response of Pressure Measuring Systems. NLR-TR F. 238.

Bonitz, S., Larsson, L., Sebben, S., 2018. Unsteady pressure analysis of the near wall flow downstream of the front wheel of a passenger car under yaw conditions. Int. J. Heat Fluid Flow (ISSN: 0142-727X) 73, 188–198. http://dx.doi.org/10.1016/j.ijheatfluidflow.2018.07.007, (Visited on 2022-11-04).

Brandt, A., Berg, H., Bolzon, M., Josefsson, L., 2019. The effects of wheel design on the aerodynamic drag of passenger vehicles. SAE Int. J. Adv. Curr. Pract. Mob. (ISSN: 2641-9637) 1 (3), 1279–1299. http://dx.doi.org/10.4271/2019-01-0662, (Visited on 2020-04-07).

Cogotti, A., 1983. Aerodynamic characteristics of car wheels. Int. J. Veh. Des..

Croner, E., Bézard, H., Sicot, C., Mothay, G., 2013. Aerodynamic characterization of the wake of an isolated rolling wheel. Int. J. Heat Fluid Flow (ISSN: 0142727X) 43, 233–243. http://dx.doi.org/10.1016/j.ijheatfluidflow.2013.04.008, (Visited on 2020-04-09).

De Gregorio, F., Visingardi, A., 2020. Vortex detection criteria assessment for PIV data in rotorcraft applications. Exp. Fluids (ISSN: 1432-1114) 61 (8), 179. http://dx.doi.org/10.1007/s00348-020-03012-7, (Visited on 2023-05-15).

Fackrell, J.E., Harvey, J.K., 1973. The flow field and pressure distribution of an isolated road wheel. In: Advances in Road Vehicle Aerodynamics, Vol. 10. pp. 155–165.

Graftieaux, L., Michard, M., Grosjean, N., 2001. Combining PIV, POD and vortex identification algorithms for the study of unsteady turbulent swirling flows. Meas. Sci. Technol. (ISSN: 0957-0233) 12 (9), 1422–1429. http://dx.doi.org/10.1088/0957-0233/12/9/307, (Visited on 2022-08-23).

Gray, M., Kuthada, T., Chang, J.H., Kim, H.-L., Lee, E., Park, M., 2019. Improved methodology for realistic representation of rotating wheels in CFD applications. In: Progress in Vehicle Aerodynamics and Thermal Management. Stuttgart.

Hirose, K., Kawamata, H., Oshima, M., 2019. Aerodynamic sensitivity analysis of wheel shape factors. SAE Int. J. Adv. Curr. Pract. Mob. 1 (3), 1300–1310. http://dx.doi.org/10.4271/2019-01-0667, (Visited on 2020-04-07).

Josefsson, E., 2022. Tyre Aerodynamics of Passenger Vehicles (Licentiate Thesis). Chalmers University of Technology.

Josefsson, E., Hobeika, T., Sebben, S., Urquhart, M., 2022. Investigation of tyre pattern effect on the aerodynamics of a passenger vehicle. J. Fluids Eng. (ISSN: 0098-2202) 144 (11), http://dx.doi.org/10.1115/1.4054851, (Visited on 2022-07-07).

Landström, C., Josefsson, L., Walker, T., Löfdahl, L., 2012. Aerodynamic effects of different tire models on a Sedan Type Passenger Car. SAE Int. J. Passeng. Cars - Mech. Syst. (ISSN: 1946-4002) 5 (1), 136–151. http://dx.doi.org/10.4271/2012-01-0169, (Visited on 2021-11-29).

Ljungskog, E., Sebben, S., Broniewicz, A., 2019a. Inclusion of the physical wind tunnel in vehicle CFD simulations for improved prediction quality. J. Wind Eng. Ind. Aerodyn. (ISSN: 0167-6105) 197, http://dx.doi.org/10.1016/j.jweia.2019.104055, (Visited on 2020-04-16).

Ljungskog, E., Sebben, S., Broniewicz, A., 2019b. Uncertainty quantification of flow uniformity measurements in a Slotted Wall Wind Tunnel. In: WCX SAE World Congress Experience. SAE International, Detroit, Michigan, United States, http://dx.doi.org/10.4271/2019-01-0656.

Mlinaric, P., 2007. Investigation of the Influence of Tyre Deformation and Tyre Contact Patch on CFD Predictions of Aerodynamic Forces on a Passenger Car (MA thesis). Chalmers University of Technology, Gothenburg.

Parfett, A., Babinsky, H., Harvey, J.K., 2022. A study of the time-resolved structure of the vortices shed into the wake of an isolated F1 car wheel. Exp. Fluids (ISSN: 1432-1114) 63 (7), 116. http://dx.doi.org/10.1007/s00348-022-03458-x, (Visited on 2022-08-16).

Patel, D., Garmory, A., Passmore, M., 2022. On the wake of an isolated rotating wheel: An experimental and numerical investigation. J. Wind Eng. Ind. Aerodyn. (ISSN: 0167-6105) 227, http://dx.doi.org/10.1016/j.jweia.2022.105049, (Visited on 2022-07-04).

Pavlovic, J., Marotta, A., Ciuffo, B., 2016. CO2 emissions and energy demands of vehicles tested under the NEDC and the new WLTP type approval test procedures. Appl. Energy (ISSN: 0306-2619) 177, 661–670. http://dx.doi.org/10.1016/j.apenergy.2016.05.110, (Visited on 2022-06-29).

Sterken, L., Sebben, S., Walker, T., Löfdahl, L., 2014. Effect of the traversing unit on the flow structures behind a passenger vehicle. In: IMechE International Vehicle Aerodynamics Conference.

Sternéus, J., Walker, T., Bender, T., 2007. Upgrade of the Volvo Cars Aerodynamic Wind Tunnel. SAE Technical Paper 2007-01-1043, http://dx.doi.org/10.4271/2007-01-1043, (Visited on 2021-03-15).

Swedac, 2020. Ackrediteringsnr: 1375. URL: https://search.swedac.se/sv/ackrediteringar/1375/a000753-004 (visited on 2022-03-24).

Wäschle, A., 2007. The Influence of Rotating Wheels on Vehicle Aerodynamics - Numerical and Experimental Investigations. SAE Technical Paper 2007-01-0107, http://dx.doi.org/10.4271/2007-01-0107, (Visited on 2020-04-03).

Wickern, G., Zwicker, K., Pfadenhauer, M., 1997. Rotating wheels - Their Impact on Wind Tunnel Test Techniques and on vehicle drag results. SAE Trans. 254–270. http://dx.doi.org/10.4271/970133, (Visited on 2020-05-14).

Wiedemann, J., 1996. The influence of ground simulation and wheel rotation on aerodynamic drag optimization - Potential for reducing fuel consumption. SAE Trans. (ISSN: 0096-736X) 105, 810–819, arXiv:44720798 URL: https://www.jstor.org/stable/44720798 (visited on 2022-07-05).

Wittmeier, F., Kuthada, T., Widdecke, N., Wiedemann, J., 2014. Model Scale Based Process for the Development of Aerodynamic Tire Characteristics. SAE Technical Paper 2014-01-0585, http://dx.doi.org/10.4271/2014-01-0585, (Visited on 2021-08-31).

Wittmeier, F., Widdecke, N., Wiedemann, J., Lindener, N., Armbruster, R., 2013. Tyre development from an aerodynamic perspective. ATZ Worldwide (ISSN: 2192-9076) 115 (2), 42–48. http://dx.doi.org/10.1007/s38311-013-0022-x, (Visited on 2022-06-29).